

Supporting Information

An 18-connected wheel-shaped molybdenum(V) nickel-phosphate cluster for photoelectrochemical sensing of levofloxacin

Jie-Fei Wang, Chun-Xiao Yin, Jia-Xin Qi, Yuan-Yuan Ma*, Zheng-Guo Lin* and Zhan-Gang Han*

Hebei Technology Innovation Center for Energy Conversion Materials and Devices, National Demonstration Center for Experimental Chemistry Education, College of Chemistry and Materials Science, Hebei Normal University, Shijiazhuang, Hebei 050024, P. R. China.

E-mail: mayy334@hebtu.edu.cn, linzhengguo11@163.com, hanzg116@126.com

I. Experimental Section

All chemical reagents were obtained through commercial channels, and were used as received. Ultrapure water (18.25 M Ω cm) was obtained from a Sichuan-water-purifier physical and chemical analysis type water purifier (Sichuan, China) was used throughout the experiments unless otherwise noted. Na₆Ni₆[(Mo₂O₄)₈Ni₁₆(H₂PO₄)₄(HPO₄)₁₀(PO₄)₁₂(OH)₆(H₂O)₈]•66H₂O (abbr. Mo₁₆Ni₁₆P₂₄) was synthesized according to the previous reports.¹

Synthesis of compound 1

A mixture of Na₂MoO₄·2H₂O (0.10 g, 0.49 mmol), btmbi (0.04 g, 0.126 mmol), NiCl₂·6H₂O (0.2 g, 0.84 mmol), H₃PO₄ (0.50 mL, 7.50 mmol), and H₂O (8.00 mL, 0.44 mol) was stirred for 30 min, and the pH was adjusted to 1.5 with NaOH. The final mixture was placed in a Parr Teflon-lined stainless steel vessel (20 mL) under autogenous pressure and heated at 160 °C for 5 d. Yellow crystals were obtained, which were washed with distilled water and air dried to give a yield of 38.6% (based on Mo).

Instruments and measurements

The scanning electron microscopy (SEM) was performed on a Phenom-Workstation\ThermoFisher. The FT-IR spectrum (KBr precipitation) in the range of 4000~400 cm⁻¹ was recorded with an FTIR-8900 infrared spectrometer. Powder X-ray diffraction (XRD) was performed on a Bruker AXSD8 Advance diffractometer. X-ray photoelectron spectroscopy (XPS) was performed on a AXIS ULtra DLD Advance diffractometer.

Thermogravimetric (TG) analysis was carried out with a PerkinElmer Pyris Diamond TG Instruments. The UV-vis diffuse-reflectance spectroscopy (UV-vis DRS) spectra were characterized using an Agilent Cary 5000 UV-vis spectrophotometer with barium sulfate (BaSO₄) as the standard. All photoelectrochemical tests were completed using CHI760E workstation.

X-ray crystallography

Reliable diffraction data were collected using a XtaLAB Synergy, Dualflex, HyPix diffractometer with Cu K α monochromated radiation (λ = 1.5418 Å) at 297.0(4) K. Using Olex2², the structure was solved with the SHELXT³ structure solution program using Intrinsic Phasing and refined with the SHELXL⁴ refinement package using Least Squares minimisation. The CCDC code is 2403791 for compound 1.

Preparation of working electrode modified with compound 1

In order to enhance the conductivity of the crystal, 12 mg of crystal was first mixed and grinded with carbon black under mass ratios of 1:2, and then dispersed into 200 μ L of 0.5 wt % Nafion solution and ultrasonicated for 40 min to obtain a uniformly dispersed solution. Then, 78 μ L of catalyst suspension was dropped on the surface of

protecting agent to ensure that the hybrids catalysts can be tightly modified on the surface of carbon paper.

Photoelectrochemical detection of LVF

All the photoelectrochemical detection experiments were conducted on the CHI760E photoelectrochemical workstation using a three-electrode system in 0.5 M H₂SO₄ (pH = 0). Cyclic voltammetry (CV) and photoelectrochemical impedance spectroscopy (EIS) were used to characterize the photoelectrochemical properties of compound **1**. EIS was tested at a frequency of 100 kHz to 1 Hz. The differential pulse voltammetry (DPV) technique was used to evaluate the photoelectrochemical LVF detection performance, the potential window was set in the range of -0.1 ~ 0.8 V with amplitude of 50 mV. The limit of detection of compound **1** was calculated according to the principle of S/N = 3. The relative standard deviation was calculated by using 15 cycles blank experiments. The detection sensitivity was obtained by linearly fitting the curves of LVF concentration and corresponding peak currents. The formula $I_{cat} / I_L = (\pi k_{cat} ct)^{1/2}$, where I_{cat} represents the catalytic current after adding LVF, I_L is the diffusion-limited current in the blank solution, t is the elapsed time(s), c is the concentration of the LVF solution, and k_{cat} is the catalytic rate constant. The Cottrell equation ($I = nFAD^{1/2}c\pi^{1/2}t^{1/2}$), the diffusion coefficient of LVF on compound **1** was investigated. In this equation, D represents the diffusion coefficient (cm²·s⁻¹), n is the number of transferred electrons (2), A is the electrode area (0.5 cm²), I is the peak current dominated by the diffusion of LVF from the electrolyte to the electrolyte interface, and c is the concentration of added LVF (mol·L⁻¹).

When applied compound **1** in a milk sample for LVF detection, it is used as a solvent instead of ultrapure water to prepare a 0.5 M sulfuric acid solution, which is then used as an electrolyte solution.

II. Supplementary structural figures.

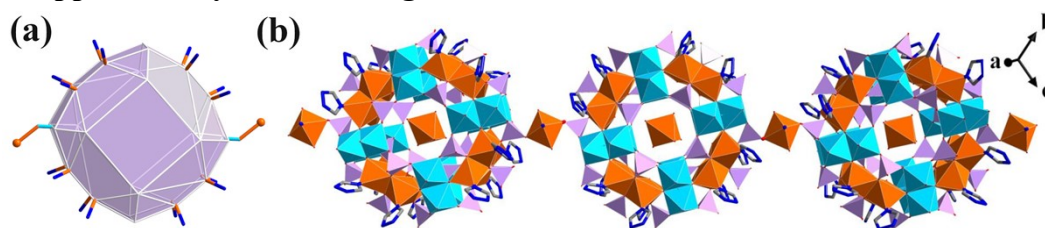


Fig. S1. (a) Schematic view of 18-connected $\{\text{Mo}_{16}\text{Ni}_{16}\text{P}_{24}\}$ cluster. (b) 1-D chain based on $\{\text{Mo}_{16}\text{Ni}_{16}\text{P}_{24}\}$ clusters.

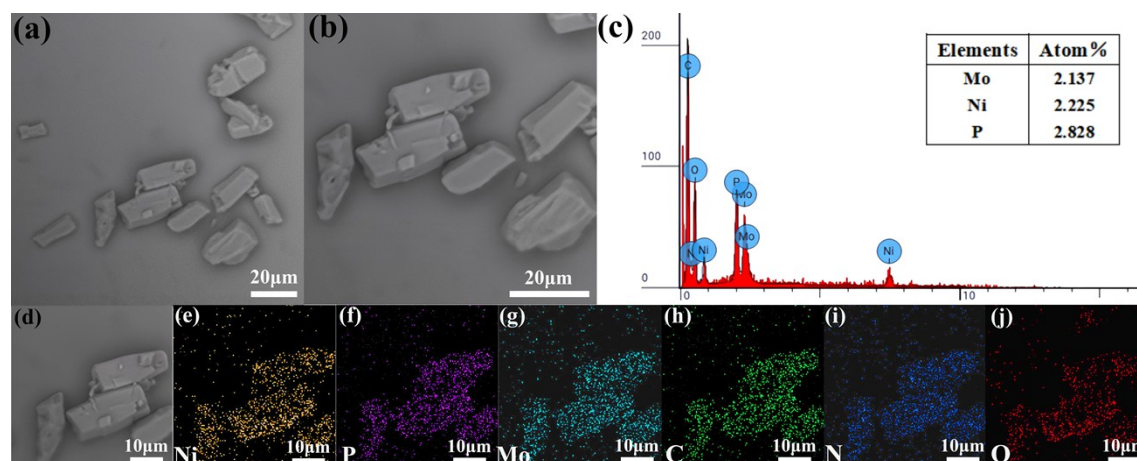


Fig. S2. SEM images (a-b), EDS spectrum (c) and elemental mapping images (d-j) of compound **1**.

The morphology and elemental composition of compound **1** were characterized by scanning electron microscopy (SEM) and energy dispersive spectroscopy (EDS). As shown in Fig. S2, compound **1** displayed hexagonal prism shaped morphology. The EDS spectrum shows the existence of the Mo, Ni, P, C, N and O elements, and the elemental ratio of Mo, Ni and P conforms to that in the crystal structure. The elemental mapping images indicate that the elements are well dispersed on the surface of compound **1**.

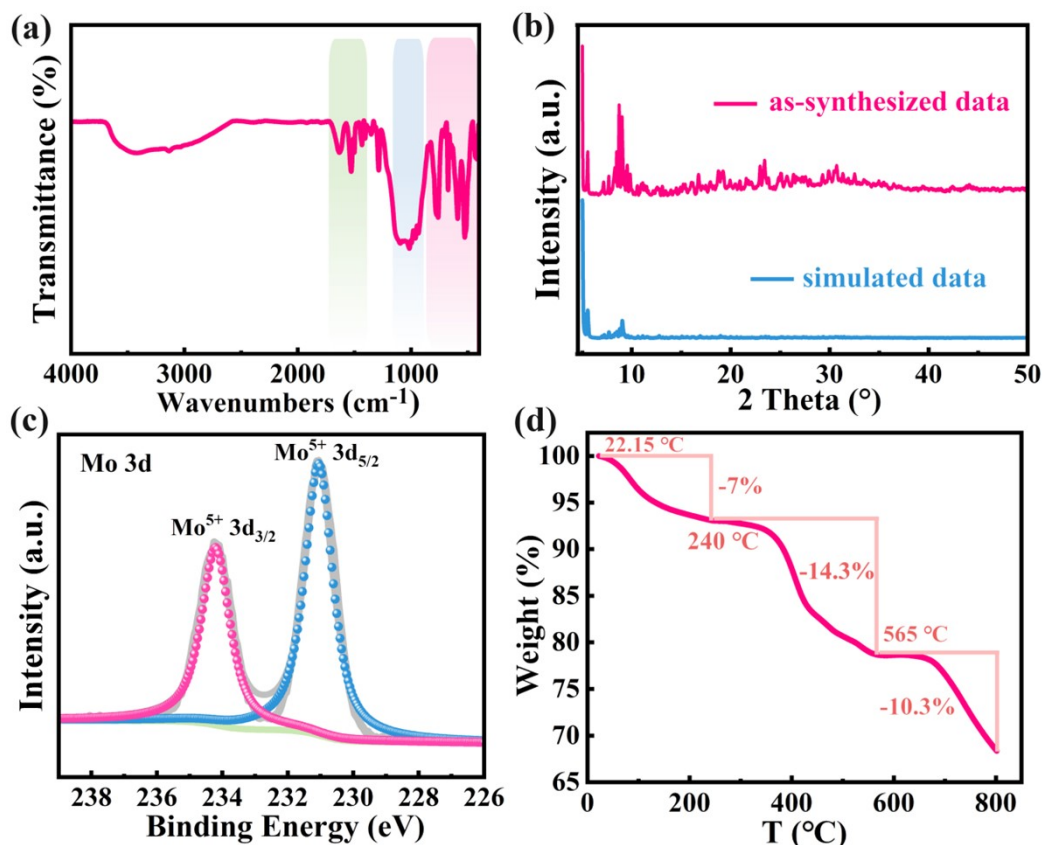


Fig. S3. (a) IR spectrum of compound **1**. (b) The simulated and calculated XRD patterns of compound **1**. (c) The high-resolution XPS spectrum of Mo in compound **1**. (d) The TG curves of compound **1**.

The IR spectrum presents the characteristic bands of $\{\text{Mo}_{16}\text{Ni}_{16}\text{P}_{24}\}$ cluster and btmbi ligand (Fig. 3a). The characteristic peak of the molybdenum-oxygen bond appears in the low wavenumber region below 1000 cm^{-1} , while the characteristic peak of the phosphorus-oxygen bond is located in the mid-wavenumber region of $1000\sim 1100\text{ cm}^{-1}$. The peaks observed in the range of $1520\sim 1640\text{ cm}^{-1}$ are attributed to C=C and C=N in the btmbi ligand (Fig. S3a). XRD patterns of as-synthesized compound **1** match well with the calculation result, indicating good phase purity and high crystallinity. Fig. S3c shows the XPS spectra of Mo and Ni elements in compound **1**. In the Mo 3d XPS spectrum, the binding energies at 231.02 and 234.12 eV are assigned to the 3d_{5/2} and 3d_{3/2} signals of MoV, respectively. The Ni 2p XPS spectrum shows that the Ni species in compound **1** are in +2 oxidation state. This result also aligns well with the bond valence sum calculation results (Table S4, ESI†). Such full-reduced feature of $\{\text{Mo}_{16}\text{Ni}_{16}\text{P}_{24}\}$ cluster will endow compound **1** with wide spectral absorption and excellent redox property, making it a promising photo-electrocatalytic material.

TG analysis indicates that compound **1** has high thermal stability and can maintain its structure up to $240\text{ }^{\circ}\text{C}$ (Fig. S3d). The TG curve reveals three distinct weight loss stages corresponding to the loss of water molecules and organic components from compound **1**. In the first stage, between 22.15°C and 240°C ,

compound **1** loses 24 crystalline water molecules and 8 coordinated water molecules, resulting in an actual weight loss of 7.0% (comparable to the theoretical weight loss of 7.1%). In the second stage, from 240°C to 565°C, partial decomposition of the organic ligand btmbi occurs, leading to an actual weight loss of 14.3% (lower than the theoretical weight loss of 31.1%). In the third stage, between 565°C and 800°C, further decomposition of most of the organic ligand btmbi takes place, resulting in an additional weight loss of 10.3%. The total weight loss over these three stages is 24.6% (Fig. S3d).

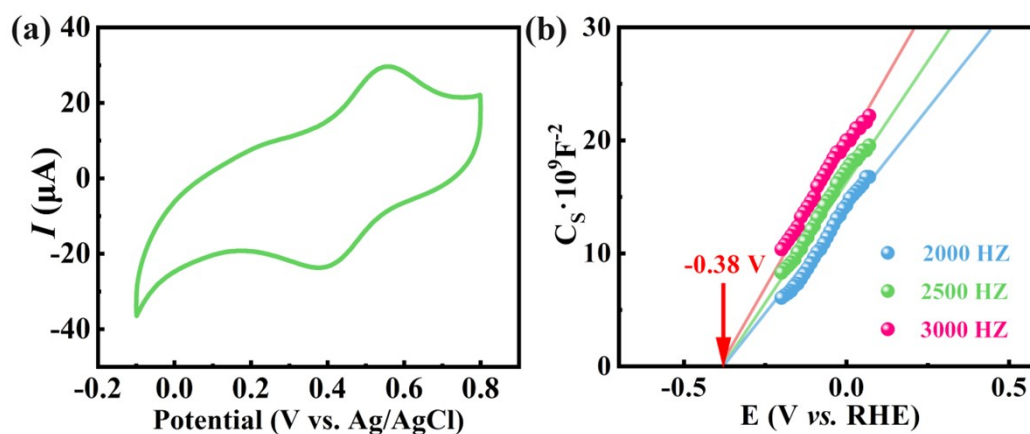


Fig. S4. (a) CV curve of btmbi ligand. (b) Mott-Schottky plots of $\{\text{Mo}_{16}\text{Ni}_{16}\text{P}_{24}\}$ salt in 0.2 M Na_2SO_4 solution at $\text{pH} = 6.80$.

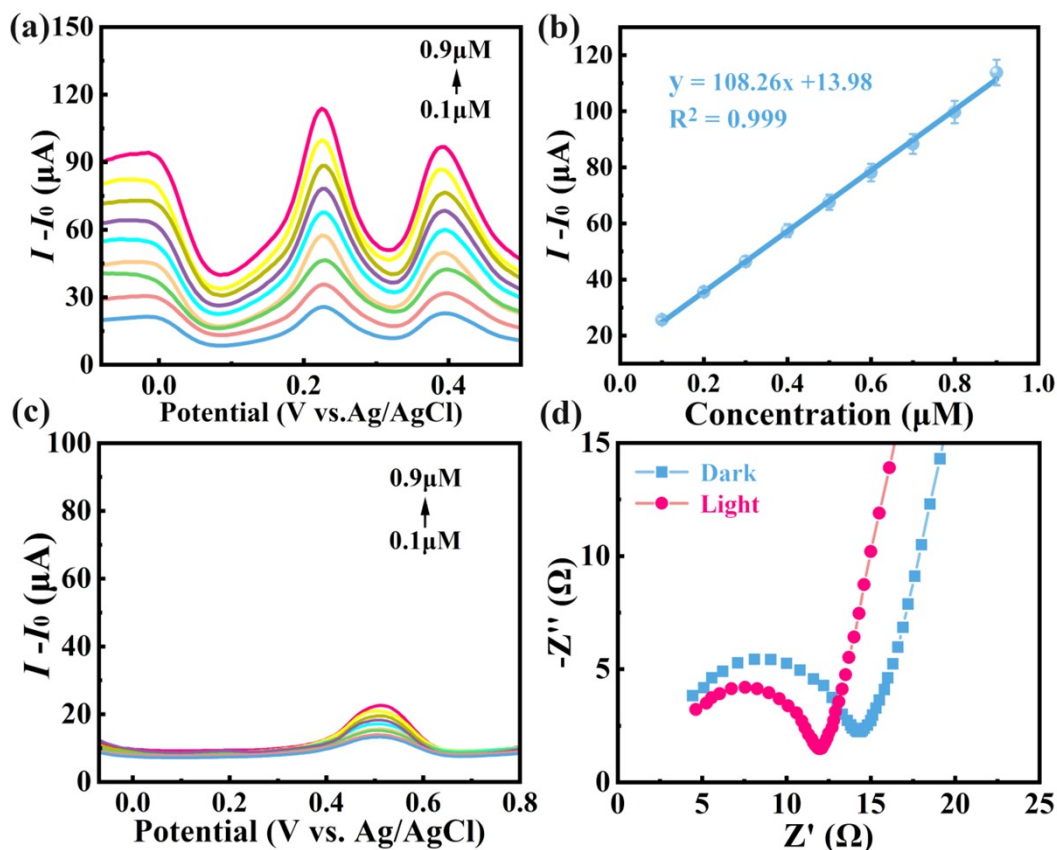


Fig. S5. (a) DPV curves of $\{Mo_{16}Ni_{16}P_{24}\}$ salt in 0.5 M H_2SO_4 with the successive changes of 0.1-0.9 μM LVF under visible light illumination. (b) The linear dependence curve of light. (c) DPV curves of btmbi ligand in 0.1-0.9 μM LVF. (d) EIS spectras of compound 1 in dark and light-irradiation condition.

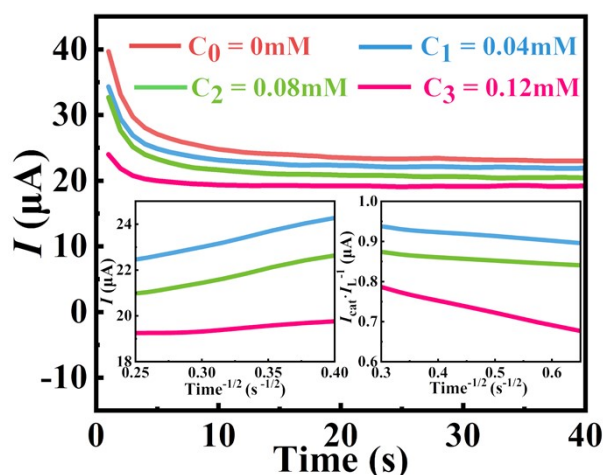


Fig. S6. Chronoamperometry on compound 1 after the addition of different concentrations of LVF in 0.5 M H_2SO_4 . Inset left: I versus $t^{1/2}$; right: plots of I_{cat}/I_L versus $t^{1/2}$.

To gain a deeper understanding of the catalytic mechanism during the electrooxidation of LVF, chronoamperometry was employed for analysis. The

resulting $i-t$ curves for various LVF concentrations were plotted to track the changes over time. By applying the formula $I_{\text{cat}} / I_{\text{L}} = (\pi k_{\text{cat}} ct)^{1/2}$, the relationship between the catalytic current and reaction time was established, yielding a catalytic rate constant k_{cat} of $19.10 \text{ mol}^{-1} \cdot \text{s}^{-1}$. This value signifies that compound **1** possesses high electrocatalytic activity towards the oxidation of LVF. Utilizing the Cottrell equation ($I = nFAD^{1/2}c\pi^{1/2}t^{1/2}$), the diffusion coefficient D was calculated to be $1.97 \times 10^{-6} \text{ cm}^2 \cdot \text{s}^{-1}$, which further underscores the superior diffusion kinetics of LVF on the surface of compound **1** (Fig. S6).

The possible reaction mechanism for LVF detection were proposed. The related reactions are listed in equations S1-S3.

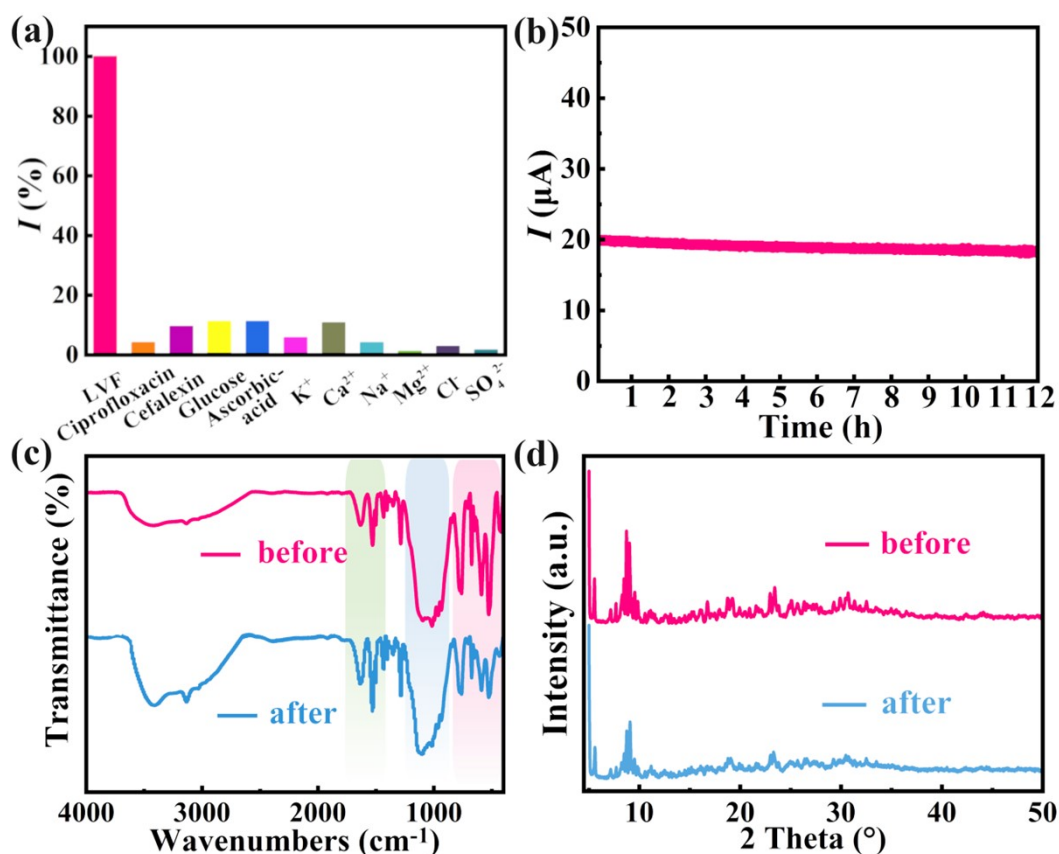
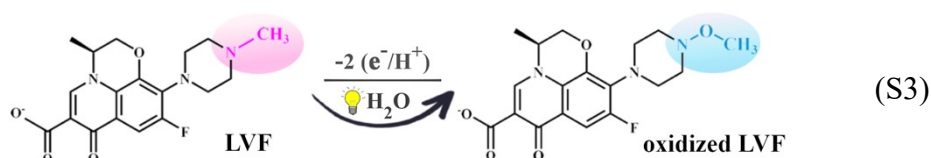


Fig. S7. (a) Percentage changes in response signal to the addition of different interfering ion (500 μM) in detection system. (b) Stability of amperometric responses to 50 μM LVF in 0.5 M H₂SO₄ electrolyte. (c) Comparison of IR of compound **1**

before and after catalysis reaction. (d) Comparison of XRD of compound **1** before and after catalysis reaction.

III. Supplementary structural tables

Table S1. Crystal data and structure refinement details for compound **1**.

Crystal	Compound 1
Empirical formula	$C_{72.25}H_{78.5}Mo_8N_{24}Ni_9O_{70}P_{12}$
Formula weight	4070.64
Crystal System	Triclinic
Space group	$P-1$
a (Å)	19.5356(11)
b (Å)	20.8084(9)
c (Å)	21.3316(7)
α, β, γ (°)	112.614(4), 102.679(4), 104.922(4)
Volume (Å ³), Z	7224.9(6), 2
Density(calculated)(mg·m ⁻³)	1.871
Absorption coefficient(mm ⁻¹)	8.808
$F_{(000)}$	4016.0
Crystal size (mm ³)	0.2 × 0.15 × 0.14
2θ (°)	4.804 to 129.996
Reflections collected	94673
Independent reflections ($R_{(int)}$)	24525 [$R_{(int)} = 0.1342$]
Max and min. transmission	1.000 and 0.863
Data/restraints/parameters	24525/7222/1722
Goodness-of-fit on F^2	1.133
Final R indices [$I > 2\sigma(I)$] ^a	$R_1 = 0.1120$, $wR_2 = 0.3063$
R indices (all data)	$R_1 = 0.1629$, $wR_2 = 0.3466$

Table S2. Selective bond lengths (Å) and bond angles (°) of compound **1**.

Mo1-O1	2.035(11)	Ni2-O56	2.020(12)	O1-Mo1-O22	80.9(5)	O15-Ni7-N9 ⁱⁱⁱ	90(6)
Mo1-O30	1.958(13)	Ni2-O66	2.191(13)	O30-Mo1-O24	159.7(5)	N19 ⁱⁱ -Ni2-O10	97.7(6)
Mo1-O34	1.674(12)	Ni2-O72	2.008(12)	O1-P1-O4	114.2(7)	N7 ⁱⁱⁱ -Ni3-O45	102.2(9)
P1-O1	1.512(12)	Ni2-N19 ⁱⁱ	2.027(10)	O4-P1-O19	106.6(7)	Ni13-O42-Ni9 ⁱ	100.5(5)
P1-O19	1.562(14)	Ni3-N7 ⁱⁱⁱ	2.007(17)	O53-Ni7-O15	87.4(6)	Ni10 ⁱ -O4-Ni6	96.3(5)
Ni4-O8	1.970(12)	Ni4-N8 ⁱⁱⁱ	1.988(9)	O42-Ni3-O41	96.7(5)	N9 ⁱⁱⁱⁱ -Ni7-N9 ⁱⁱⁱ	180(10)
Ni6-O50	2.229(12)	Ni5-N13	2.012(11)	O8-Ni4-O3	169.4(6)	P14-O72-Ni2	122.3(9)
Ni7-O15 ⁱⁱⁱⁱ	2.089(19)	Ni7-N9 ⁱⁱⁱ	2.10(6)	O15-Ni7-O15 ⁱⁱ	180.0	P1-O1-Mo1	143.6(7)
Ni2-O10	2.141(14)	C7-C69	1.45(4)	O72-Ni2-N19 ⁱⁱ	86.6(6)	Mo6-O8-Ni4	133.7(6)
Ni2-O39	2.104(14)	N15-C91	1.542(10)	O8-Ni4-N8 ⁱⁱⁱ	85.5(6)	C49-N1-Ni10	129.0(11)

i: 1-X,1-Y,1-Z; ii: -1+X,+Y,+Z; iii:1+X,+Y,+Z; iiiii:1-X,-Y,-Z; iiiiii: -X,-Y,-Z; iiiiii: 2-X,1-Y,1-Z

Table S3. Hydrogen bonding lengths (Å) and angles (°) of compound **1**.

D-H...A	D-H	H...A	D...A	∠D-H...A	D-H...A	D-H	H...A	D...A	∠D-H...A
O17-H17A...O40	0.91	1.93	2.61(3)	131	C33-H33...O30	0.93	2.18	2.66(4)	111
O71-H71A...O40	0.89	1.81	2.53(4)	136	C33-H33...O34	0.93	2.56	3.48(5)	168
N20-H20...N14	0.86	2.43	3.02(2)	126	C33-H33...O54	0.93	2.56	3.12(4)	119
C1-H1...O63	0.93	2.45	3.29(3)	151	C42-H42...O21	0.93	2.58	3.18(3)	123
C6-H6...O43	0.93	2.28	3.19(2)	165	C49-H49...O59	0.93	2.58	3.35(3)	140
C12-H12...O33	0.93	2.43	3.23(2)	144	C60-H60A...O54	0.97	2.45	3.38(3)	160
C14-H14...O38	0.93	2.47	2.901(18)	108	C65-H65B...O37	0.97	2.29	3.18(3)	152
C18-H18...O72	0.93	2.44	2.82(2)	104	C74-H74...O51	0.93	2.50	3.27(2)	140
C22-H22...O49	0.93	2.18	3.027(18))	150	C80-H80...O64	0.93	2.46	2.84(3)	105
C24-H24...O70	0.93	1.99	3.87(2)	157	C80-H80...O68	0.93	2.57	3.25(4)	130
C26-H26...O23	0.93	2.16	2.85(3)	131	C70-H70...N6	0.93	2.55	2.87(2)	101

Table S4. BVS calculation results of atoms.

Compound	Mo1	Mo2	Mo3	Mo4	Mo5	Mo6	Mo7	Mo8
1	5.42	5.41	5.20	5.54	5.36	5.41	5.03	5.42

Table S5. Peak potential data (mV) for compound **1** at a sweep rate of 130 mV • s⁻¹

Scan rate	<i>E_a/E_c</i> (I) / mV	<i>E_a/E_c</i> (II) / mV	<i>E_a/E_c</i> (III) / mV
	130 mV • s ⁻¹	0/-46	232/203
	<i>E</i> _{1/2}	<i>E</i> _{1/2}	<i>E</i> _{1/2}
	-23	217.5	370

Table S6. Comparison of compound **1** with other reported modified materials for the determination of LVF.

Modified materials	Method	LOD (μM)	Refs
Compound 1	DPV	0.00646	This work
SPS (In ₂ S ₃ /In ₂ O ₃ /MIP)	i-t	0.000047	[5]
α-ZrP/NG/GCE	SDLSV	0.0026	[6]
SrV/GCN/GCE	DPV	0.028	[7]
AgNPs-CB-PEDOT:PSS/GCE	SWV	0.014	[8]
Co@CaHPO/GCE	LSV	0.151	[9]

References

1. C. du Peloux, A. Dolbecq, P. Mialane, J. Marrot, E. Rivière and F. Sécheresse, *Inorg. Chem.*, 2002, **41**, 7100-7104.
2. O. V. Dolomanov, L. J. Bourhis, R. J. Gildea, J.A.K. Howard and H. Puschmann, *J. Appl. Crystallogr.*, 2009, **42**, 339-341.
3. G. M. Sheldrick, *Acta Crystallogr A*, 2015, **71**, 3-8.
4. G. M. Sheldrick, *Acta Crystallogr C*, 2015, **71**, 3-87304.
5. Z. Zhu, X. Bai and Y. Ji, *Sens. Actuators. B. Chem.*, 2023, **377**, 133076.
6. G. Li, X. Wan, Y. Xia, D. Tuo, X. Qi, T. Wang, M. Mehmandoust, N. Erk, Q. He and Q. Li, *ACS Appl. Nano Mater.*, 2023, **6**, 17040-17052.
7. N. Nataraj, S. Chen and S. Krishnan, *Environ. Sci-Nano*, 2022, **9**, 3927-3942.
8. A. Wong, A. Santos and O. Filho, *Sens. Actuators. B. Chem.*, 2018, **255**, 2264-2273.
9. K. Alagumalai, S. Palanisamy, P. Kumar, N. ElNaker, S. Kim, M. Chiesa and P. Prakash, *Environ. Pollut.*, 2024, **343**, 123189.